SECONDARY PARTICLE BACKGROUND LEVELS AND EFFECTS ON DETECTORS AT FUTURE HADRON COLLIDERS

TRIVAN PAL
Physics Research Division,
Superconducting Super Collider Laboratory, 2550 Beckleymeade Avenue*
Dallas, Texas 75237

1. INTRODUCTION

The next generation of hadron colliders, the Superconducting Super Collider (SSC) and the Large Hadron Collider (LHC), will operate at high center-of-mass energies and luminosities. Namely, for the SSC (LHC) $\sqrt{s} = 40$ TeV ($\sqrt{s} = 16$ TeV) and $\mathcal{L} = 10^{33}$ cm^{-2}s^{-1} ($\mathcal{L} = 3 \times 10^{34}$ cm^{-2}s^{-1}). These conditions will result in the production of large backgrounds as well as radiation environments. Ascertaining the backgrounds, in terms of the production of secondary charged and neutral particles, and the radiation environments are important considerations for the detectors proposed for these colliders. An initial investigation of the radiation levels in the SSC detectors was undertaken by D. Groom and colleagues, in the context of the "task force on radiation levels in the SSC interaction regions."[1] The method consisted essentially of an analytic approach, using standard descriptions of average events in conjunction with simulations of secondary processes.

Following Groom's work, extensive Monte Carlo simulations were performed to address the issues of backgrounds and radiation environments for the GEM[2] and SDC[3] experiments proposed at the SSC, and for the ATLAS[4] and CMS[5] experiments planned for the LHC. The purpose of the present article is to give a brief summary of some aspects of the methods, assumptions, and calculations performed to date (principally for the SSC detectors), and to stress the relevance of such calculations to the detectors proposed for the study of B-physics in particular.

At the SSC, the GEM and SDC experiments will be located in the interaction regions (IRs), where the beam optics will provide a high value of the luminosity and hence small β^*. In these regions, the dominant source of background is due to the p-p collisions themselves. The interaction rate will be approximately 10^8 Hz, corresponding to the nominal luminosity of $\mathcal{L} = 10^{33}$ cm^{-2}s^{-1}. There also exist other, smaller sources of backgrounds arising from beam-gas collisions in the vacuum pipe and beam losses in the collider lattice elements. In contrast to the above, IRs are also foreseen that will have larger free space for the experiments (for example, detectors for B-physics). However, the corresponding beam optics will result in higher values of β^* and lower luminosity.[6]

*Operated by the Universities Research Association, Inc., for the U.S. Department of Energy under Contract No. DE-AC35-89ER40486.

2. SYNOPSIS OF THE ANALYTIC APPROACH

Various processes contribute to the charged and neutral particle backgrounds and the radiation levels in the experimental apparatus. The following were considered by the task force:[7] the minimum ionizing particles (MIPs) produced in the p-p collisions; photon conversions; electromagnetic and hadronic showers in the calorimeters; and albedo particles (mostly neutrons and photons) from the showers induced in the calorimeters. We note that there are other considerations to incorporate, and these are described in the next section.

2.1 Particle Production Characteristics

The p-p interaction cross sections have been measured as a function of $\sqrt{s}$ (Figure 1) at lower energies and extrapolated to the energies of interest to us. The cross sections have also been calculated using QCD, and are subject to theoretical uncertainties arising from, for example, the parametrization of the parton distributions (i.e., structure functions). It has been assumed that 1/4 of the total cross section is elastic and 3/4 of the total cross section has been assigned to the inelastic cross section (including diffractive processes). Thus, at the SSC and LHC the values assumed are: $\sigma_{\text{inel}} = 100$ mb and 84 mb, respectively.

The distribution of charged particles produced in an inelastic p-p interaction is described as a function of the pseudorapidity (η) of the particle. The pseudorapidity is defined as $\eta = -\ln(\tan\theta/2)$, where θ is the polar angle of the particle with respect to the beam axis. Figure 2 shows the differential distribution ($dN/d\eta$) obtained using the DTUJET Monte Carlo[8] for p-p collisions at $\sqrt{s} = 40$ TeV. The Monte Carlo is based on the dual parton model and incorporates both soft and hard transverse momentum processes. The distribution in Figure 2 is approximately constant over the "central rapidity plateau." This is referred to as the "height" (H) of the rapidity plateau. The dip in the distribution at $\eta = 0$ is due to a kinematical effect.

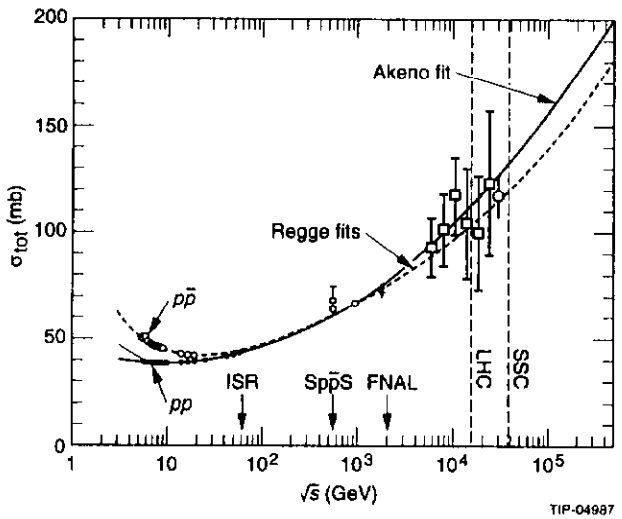

Figure 1. Data points and extrapolations to higher energies of the p-$\bar{p}$ and p-p total cross sections (Reference 9).

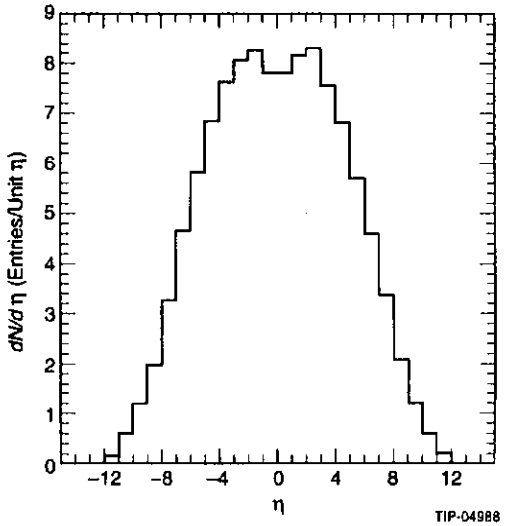

Figure 2. Distribution of charged particles as a function of the pseudorapidity, η, obtained by the DTUJET Monte Carlo. The central rapidity plateau corresponds to ~ 7.5 charged particles per unit rapidity, for p-p interactions at $\sqrt{s} = 40$ TeV.

The mean charged particle multiplicity as a function of $\sqrt{s}$ is shown in Figure 3. The lower energy data have been obtained from the ISR, SpS̄, and FNAL, and extrapolated to higher energies.[9] The value for H per unit η is 6.2 at the LHC and 7.5 at the SSC. It is observed that the momentum (p) distribution for a given value of η is an η-independent function of the transverse momentum (p_t). The studies of the task force suggest that radiation levels scale as $\langle p_t\rangle^\alpha$, where $\alpha \lesssim 1$. Furthermore, in the analytic approach the approximation $f(p_t) = \delta(p_t - \langle p_t\rangle)$ was used, which is estimated to result in a systematic error of $\sim 6\%$.[7] The (dN/dp_t) distribution for the charged particles produced in p-p collisions at $\sqrt{s} = 40$ TeV is shown in Figure 4, with $\langle p_t\rangle \sim 0.6$ GeV; whereas at LHC, $\langle p_t\rangle \sim 0.55$ GeV.

Figure 5 shows the cumulative energy fraction emitted from the interaction point (IP) as a function of η. The figure indicates typical intervals in pseudorapidity covered by the different components of the experimental apparatus, i.e., the tracking region, the barrel and end-cap regions of the calorimeter, the forward calorimeter region, and the regions of the low-beta quadrupoles, including their shielding.

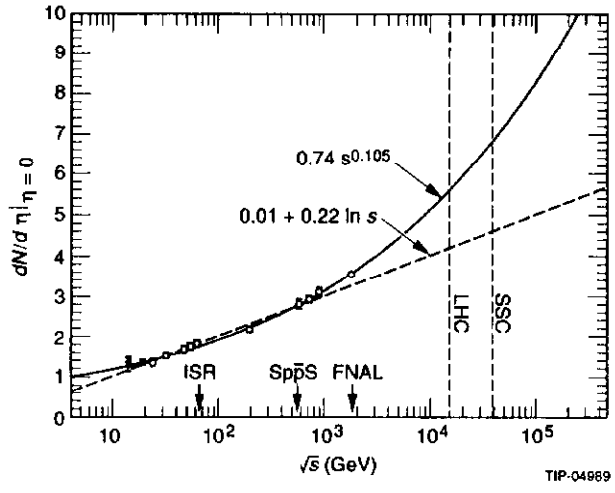

Figure 3. Evolution of the number of charged particles per unit rapidity as a function of the center-of-mass energy (Reference 9).

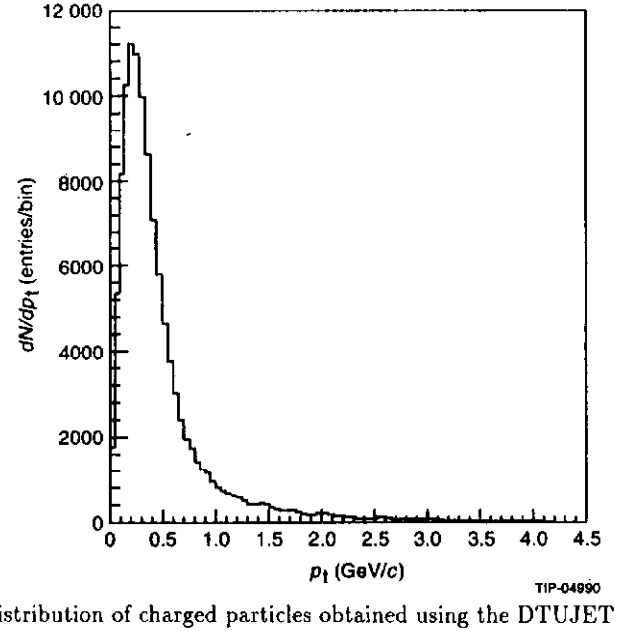

Figure 4. p_t distribution of charged particles obtained using the DTUJET Monte Carlo, for p-p interactions at $\sqrt{s} = 40$ TeV. Average p_t is approximately 0.6 GeV/c.

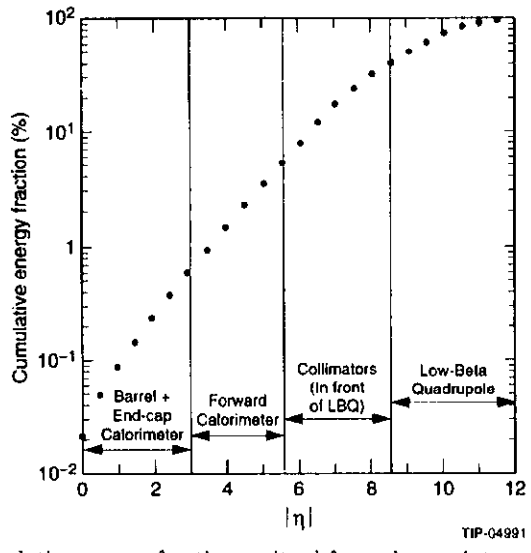

Figure 5. Cumulative energy fraction emitted from the p-p interactions at $\sqrt{s} = 40$ TeV, as a function of the pseudorapidity. Regions covered by the various detector elements are also indicated.

2.2 Quantitative Parametrizations

2.2.1 Charged Particle Flux

The charged particle flux in a unit area, A, perpendicular to the radius vector from the IP, with a polar angle θ with respect to the beam line, is given by:

$$\begin{aligned} \frac{dN}{dA} &= \left(\frac{dN}{d\eta}\right)\left(\frac{d\eta}{d\Omega}\right)\left(\frac{d\Omega}{dA}\right) \\ &= H \times \left(\frac{1}{2\pi \sin^2\theta}\right) \times \left(\frac{1}{r^2}\right) \\ &= \frac{H}{2\pi r_\perp^2}, \end{aligned} \tag{1}$$

where $d\Omega = 2\pi \sin\theta d\theta$ is the solid angle (after integration over the azimuthal angle), and $r_\perp = r \sin\theta$ is the perpendicular distance from the beam line.

2.2.2 Dose Rate

The dose rate is obtained from Eq. (1):

$$\text{Dose rate} = \frac{H \times \mathcal{L} \times \sigma_{\text{inel}}}{2\pi r_\perp^2} \times \left(\frac{dE}{dx}\right), \tag{2}$$

where $\mathcal{L} \times \sigma_{\text{inel}}$ is the event rate, and dE/dx is the usual energy loss of a particle as it goes through a thin absorber. Note that this expression does not include the effects due to

secondary interactions and photon conversions, nor low-momentum particles ascribing loops in the presence of the solenoidal magnetic fields in the tracking volume of the detectors. These effects will increase the flux, typically by a factor of two.

2.2.3 *Parametrization for Cascades*

A derivation of the ionizing dose and fluence of neutrons in a cascade process is given in Reference 9. The essential steps of the argument are as follows: from Eq. (1) and since the mean energy ($E \approx p$) of a particle at polar angle θ is $E \approx p = p_t/\sin\theta$, then the energy flow in the solid angle $d\Omega \propto 1/\sin^3\theta$, and thus the energy flow in a unit area, $dE/dA \propto 1/r^2\sin^3\theta$. Thus, one can write:

$$\text{Dose or Fluence} = \frac{C}{r^2\sin^{2+\alpha}\theta} \equiv \frac{A}{r^2}\cosh^{2+\alpha}\eta, \tag{3}$$

where C is an appropriate variable used to scale the above quantities for different colliders: $C \propto \sigma_{\text{inel}} \times \mathcal{L}_{\text{ave}} \times H \times \langle p_t \rangle^{\alpha}$. Note that $\mathcal{L}_{\text{ave}}$ is an average luminosity over the canonical 10^7 sec assumed to be the operation time for the colliders per calendar year. From the experimental data and Monte Carlo simulations, it is observed that α is in the range of $0.5 \leq \alpha < 1$.

2.2.4 *Reflections in a Cavity*

For the tracking detectors that are contained within the cavity of the calorimeters, the flux of backscattered neutrons (and photons) is an important consideration. A derivation of this albedo flux (Φ) in terms of the characteristic radius (R) of the cavity, and the average number of reflections that the neutrons undergo (A) are given in Reference 7:

$$\Phi = \frac{N}{\pi R^2}(1 + A), \tag{4}$$

where N represents the number of neutrons "injected" in the cavity. The simulation studies suggest that $(1 + A) \approx 2$ for spherical calorimeters. For neutrons, this represents the number of reflections before absorption, or degradation in energy, such that it will not damage the material (e.g., silicon for the tracker).

3. NUMERICAL TECHNIQUES

In addition to the considerations of the preceding section, we have ascertained from the extensive Monte Carlo simulations performed that the details concerning the geometry and material composition of the detector halls and the collider tunnel are also important to include. Likewise, it has been quantified by the results of the simulations that the details of the low-beta quadrupoles (LBQs) and the collimators designed to protect them (from the impinging particles produced at the IP) are rather crucial to implement, in order to predict accurately the backgrounds at various locations.

In the following sections a brief description is given of the processes involved leading to secondary particle production and radioactivation. Likewise, a summary of the various Monte Carlo codes employed to estimate the particle fluences and activity, as well as the shielding requirements, is also given.

3.1 *Summary of the Mechanisms*

Each high-energy particle interacting with a nucleus may be absorbed or may dislodge some nucleons out of the struck nucleus. In this process, additional high-energy particles can also be created. If the resulting nucleus is excited, it will de-excite by "boiling off" neutrons, also referred to as "evaporation neutrons." The nuclear reaction above is called a "star" due to the numerous particles radiating from it.

The various cross sections for producing specific nuclides depend on the target nucleus as well as on the energy and species of the incident particle. These cross sections are determined from experimental data, or else empirical formulae are employed to approximate the cross sections over orders of magnitude. Further details can be found in Reference 10. Similarly, to calculate the radioactivity, it is required to have radiological data, such as nuclear lifetimes, decay schemes, transport of β's and γ's out of the activated object (i.e., self-shielding considerations), and conversion factors that will convert the particle flux to dose.

For the Monte Carlo calculations, one has to be careful in the interpretation of the results, since these codes have low-energy cutoffs below which the particles are not followed. Depending on the cutoff, it may be higher than the thresholds of certain activation reactions. Thus, using the flux or the star density calculated by Monte Carlo would result in a lower value for the activation with respect to the true value.

Various Monte Carlo programs have been developed for the purpose of estimating the secondary particle backgrounds in terms of charged and neutral particles produced by the mechanisms described above. Likewise, there exist specific codes to calculate the radioactivity and to perform calculations to optimize the shielding required for the detectors and for personnel safety considerations. While a detailed description of the individual codes is beyond the scope of the present article, some of the salient features are listed below. The GEM and SDC experiments have used the LAHET[11] and CALOR[12] packages. Similarly, the ATLAS and CMS experiments have employed the FLUKA code.[13]

The LAHET system of codes, developed at the Los Alamos National Laboratory, consists of several "modules" for specific purposes. The transport of hadrons is done using the models of FLUKA and HETC, in the energy range < 1 MeV for charged hadrons and < 20 MeV for neutrons. The MCNP model is used for neutron transport down to thermal energies. All electromagnetic processes are simulated using the EGS code. There exists an interface to the CINDER code in order to calculate the residual radioactivity. The information of the spallation products in conjunction with the low-energy neutron spectra, calculated previously, is used to estimate the nuclide densities, activation, and dose rates as a function of the time and specific location.

The CALOR Monte Carlo package was developed at the Oak Ridge National Laboratory. The models employed consist of HETC, which uses the high-energy fragmentation scheme of FLUKA; an evaporation model for low energies; and MORSE, which is used for the transport of neutrons with kinetic energy < 20 MeV. As in the preceding case, the EGS code is used for the propagation of the electromagnetic cascades. Recently, a version of CALOR has been interfaced to the GEANT program,[14] enabling the use of a detailed detector geometry package as well as other well established features—familiar in the simulation of detector response—contained in GEANT. The combined package is called GCALOR.

In addition to the above, extensive simulations have also been performed using the MARS code.[15] In particular, since the code utilizes inclusive particle production and statistical weighting techniques, it allows for relatively fast simulation as compared to the two cases

described previously. This approach is particularly useful when considering the backgrounds produced by beam losses in the accelerator lattice elements and the transport of particles over large distances. The typical threshold energies for particle species, below which they are not followed, are: 2 MeV for charged hadrons; 0.025 eV $< E <$ 14 MeV for neutrons, and 0.1 MeV for electrons and photons.

3.2 Code Comparison and Systematics

In order to ascertain the reliability of the results obtained from the Monte Carlo calculations, it is important to compare the values with experimental data, when available, and to compare the simulation results among themselves. As an illustrative example, the test geometry shown in Figure 6 was used to calculate the neutron fluence at various locations of the setup, corresponding to punchthrough, side leakage, and albedo, which are important to quantify in the actual experiments. The energy range of the incident protons as well as the dimensions and materials used in the test geometry were selected to simulate a typical shielding requirement for the collider experiments. The comparison was performed using the three sets of simulation codes described previously: GCALOR, LAHET, and MARS. The results are summarized in Table 1. There appears to be fair agreement between the codes. The discrepancy observed between GCALOR and the other codes for the side leakage is being investigated.[16]

Another example is from the ROSTI and FLUKA collaborations[17] at CERN. The experiment was motivated by the lack of experimental information concerning the number of neutrons with energies between 0.1 MeV and 10 MeV in the cascades originating from hadrons with energy in the range 1 GeV to several hundred GeV. The ROSTI series of experiments consisted of calorimeter-like structures, constructed from 5-cm-thick slabs of iron or lead with dimensions between 30 $\times$ 30 cm^2 and 50 $\times$ 50 cm^2. In between the slabs, 6-mm-wide gaps were present that contained thin aluminium plates that were equipped with neutron activation detectors and dosimeters. From the information of these detectors, one could infer the longitudinal and radial profiles as well as the energy distribution of the neutrons. Thus, one can compare the ratios of neutrons at cascade maximum and the albedo neutrons as a function of the kinetic energy (E) of the incident primary hadron, with those of the task force.[1] These results are summarized in Table 2. The value for the ratio at cascade maximum determined from the experiment is higher than the value obtained by the task force. This would suggest an exponent $n = 0.8$ in the power law E^n, as compared to $n = 0.67$ assumed in the task force. The albedo ratio, however, is in good agreement with the value quoted by the task force.

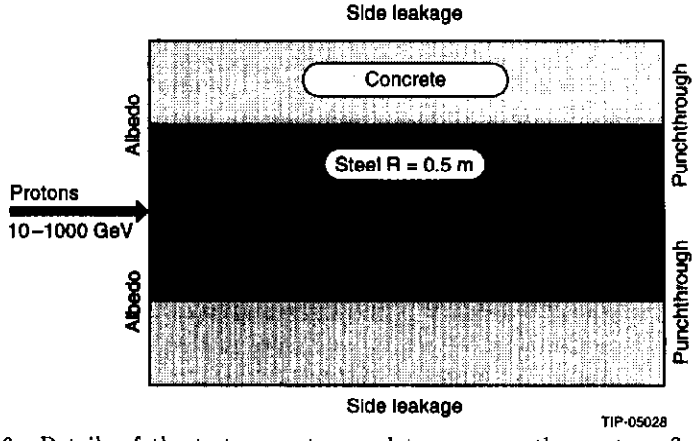

Figure 6. Details of the test geometry used to compare the neutron fluences at various locations using different Monte Carlo simulation packages.

Table 1. Results of code comparison for the test geometry shown in Figure 6. The numbers in the columns indicate the number of neutrons emerging from the surface of the cylinder per incident proton.

Incident p Energy	Monte Carlo Code	Punchthrough	Side Leakage	Albedo
10 GeV	GCALOR	0.041	1.47	32.6
	LAHET	0.027	0.72	39.2
	MARS	0.06	0.67	35.2
100 GeV	GCALOR	0.96	12.2	173.0
	LAHET	0.67	5.3	176.1
	MARS	0.96	4.2	153.5
1000 GeV	GCALOR	23.12	96.6	827.5
	LAHET	18.17	37.0	807.3
	MARS	14.75	24.1	658.1

Table 2. Comparison of fluences at cascade maximum and albedo neutrons for the ROSTI experiment and the SSCL task force.

	Cascade Maximum	Albedo
ROSTI Experiment	5.4 ± 0.1	2.8 ± 0.4
SSCL Task Force	4.1	2.9

3.3 Strategies for Shielding

The details of the shielding configurations adopted for the detectors are specific to the particular requirements. However, it is possible, albeit simplified, to list the strategy employed to design the shielding around the various sources of the backgrounds in the collider experiments, from the primary pp interactions.

There are essentially four criteria that have been identified to reduce the backgrounds:

1. to suppress the high-energy hadronic cascade by the use of dense materials;
2. to "slow down" the flux of neutrons present to thermal energies;
3. to reduce the low-energy neutron background using materials that have a high cross section for thermal neutron capture; and
4. to suppress the resulting low-energy gamma flux from the neutron capture process by using materials with high Z.

For the high-energy hadronic cascade, it is desirable to have a material with a relatively small interaction length. Likewise, the choice of the material should be such that it does not generate additional neutrons from the nuclear fission process. Taking into account practical considerations, materials such as tungsten, lead, and steel are commonly used.

Concerning the neutron flux, it is well known that hydrogen effectively shifts the energy of the neutrons downward to thermal energies, by the elastic scattering process. Thermal neutrons can also be captured by the hydrogen nucleus, producing deuterium and yielding a photon of energy 2.2 MeV. Polyethylene, for example, is a "good candidate" with the above limitation. Similarly, the Boron-10 isotope has a large cross section for neutron capture, and in the process it yields photons with energy ~ 0.4 MeV. In order to suppress the residual photon flux, high-Z materials such as lead are employed.

Figure 7(a) shows a quadrant of the GEM detector with the proposed shielding, and Figure 7(b) shows the distributions of the neutrons and photons with the shielding implemented, as estimated from the CALOR/GEANT Monte Carlo package.

In analogy, Figure 8 shows the proposed shielding for a quadrant of the SDC detector. Also indicated on the figure are the neutron and photon fluxes and their ratios for the different locations in the apparatus, obtained using the MARS and LAHET code systems.

The dimensions of the shieldings are variable, and depend on the requirements as well as the constraints present. However, the typical "size" can be estimated from the scale of the relevant figures. For both experiments, a suppression factor between 100 and 1000 has been achieved, depending on the location, by the implementation of the proposed shielding with respect to typical values of the neutron flux in the range 10^{12}–10^{13} $n/\mathrm{cm}^2/\mathrm{SSCY}$.

It is worthwhile to recall that all these calculations have been performed assuming the standard luminosity of 10^{33} $\mathrm{cm}^{-2}\mathrm{s}^{-1}$ and the canonical SSC year (SSCY) operating time of 10^7 s. It is important to stress that the desired reduction in the particle fluences (in particular neutrons and gammas) is principally motivated by the low occupancy requirements in the large-area muon detector apparatus and by the radiation damage considerations to the silicon devices in the central tracking systems.

Similar considerations have been made for the shielding requirements in the ATLAS and CMS experiments, bearing in mind that the LHC luminosity is expected to be over an order of magnitude higher ($\sim 3 \times 10^{34}$ $\mathrm{cm}^{-2}\mathrm{s}^{-1}$) than the SSC. Further details can be found in References 4 and 5.

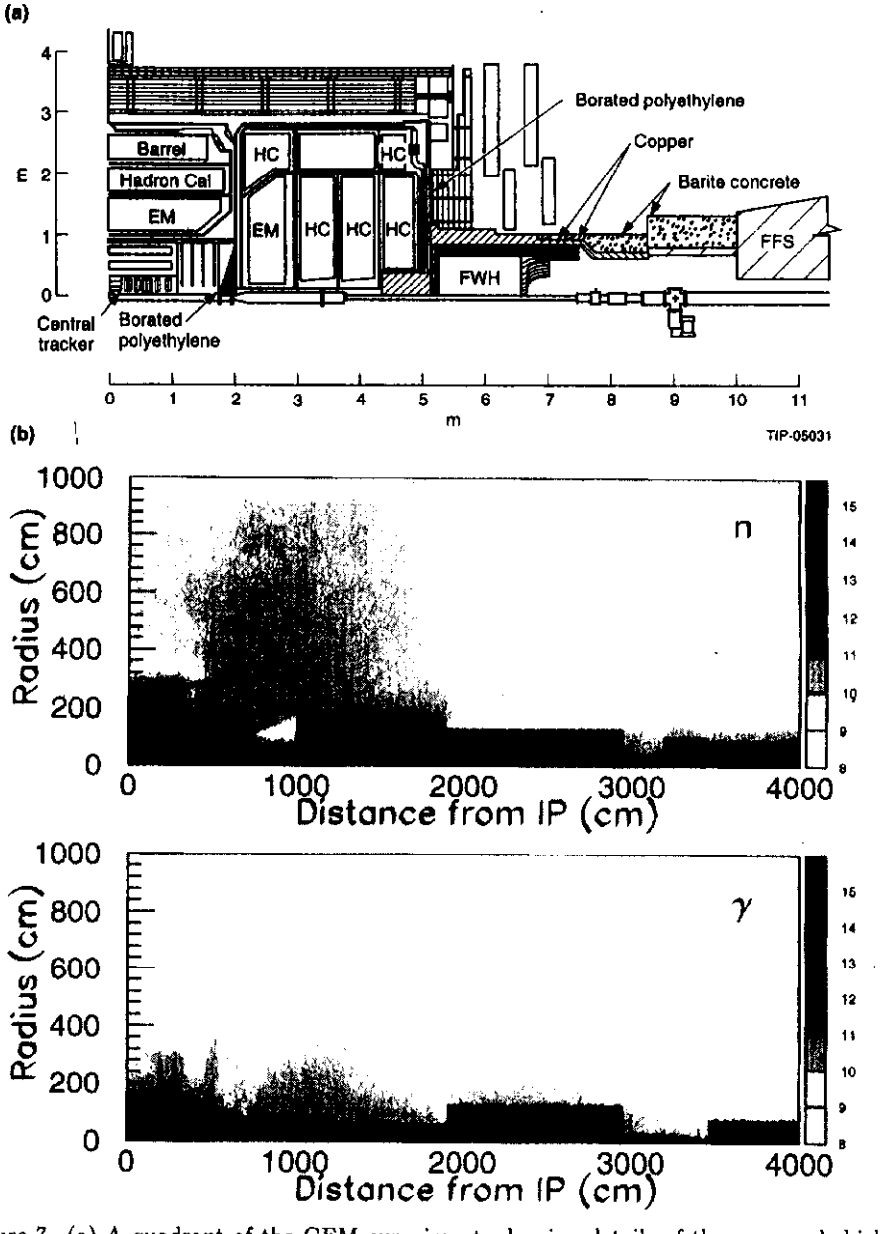

Figure 7. (a) A quadrant of the GEM experiment, showing details of the proposed shielding. (b) Results obtained for the neutron fluence and photon fluence, with the shielding implemented. The simulation code CALOR-GEANT was employed. The scale on the right-hand-side indicates the value of the exponent (m). The units are 10^m neutrons or photons per cm^2 per SSCY (Reference 2).

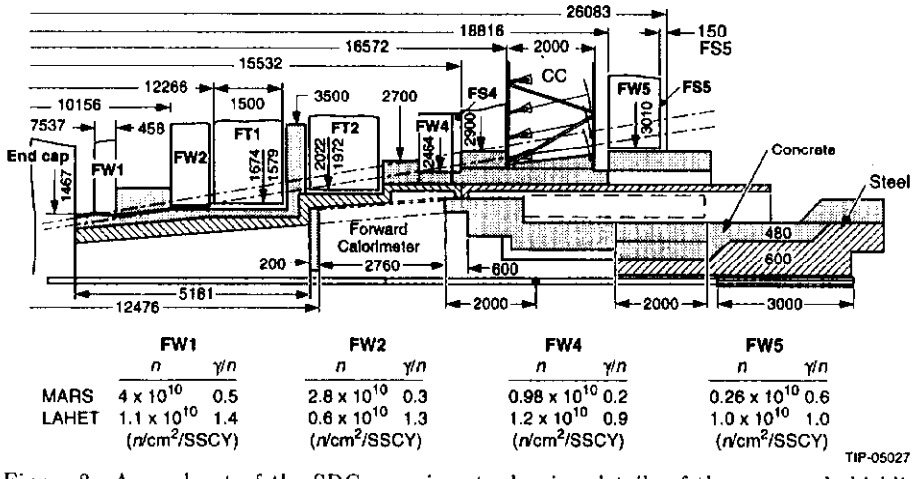

	FW1		FW2		FW4		FW5	
	n	γ/n	n	γ/n	n	γ/n	n	γ/n
MARS	4×10^{10}	0.5	2.8×10^{10}	0.3	0.98×10^{10}	0.2	0.26×10^{10}	0.6
LAHET	1.1×10^{10}	1.4	0.6×10^{10}	1.3	1.2×10^{10}	0.9	1.0×10^{10}	1.0
	(n/cm^2/SSCY)		(n/cm^2/SSCY)		(n/cm^2/SSCY)		(n/cm^2/SSCY)	

TIP-05027

Figure 8. A quadrant of the SDC experiment, showing details of the proposed shielding. The neutron and photon fluence, as well as their ratio, is also indicated at various locations of the detector, corresponding to the muon detector subsystem.

3.4 Beam-Line Considerations

From the results of the previous section it can be ascertained that among the predominant sources of backgrounds are the LBQs and the collimators on either side of the IP (at a typical distance of 25–30 m with respect to the center of the detector), as well as the beam pipe. Thus, care has been taken to optimize the design of these components. As an example, Figure 9 shows the mean number of hadronic interactions in a beam pipe as a function of the longitudinal distance along it for two geometries. In the case of the GEM apparatus, the beam pipe design[2] in the region of the central tracker consists of a beryllium section of diameter 80 mm and thickness 1.5 mm. The section of the beam pipe near the endcap calorimeter region has a larger diameter (200 mm) and is proposed to be made of stainless steel with a thickness of 2 mm. The figure serves to illustrate that the larger diameter ensures that only a small fraction of the forward emitted particles at low angles and high energies intercept the beam pipe.

Other, smaller sources of backgrounds in comparison to the particle production in the pp interaction themselves are due to beam losses in the LBQs and beam-gas interactions in the evacuated beam pipe.[18] Figure 10 shows a comparison of the magnitude of the low-energy neutron fluence from these sources. The beam loss in the LBQs is approximately 5×10^4 p/m/s in the region shown in Figure 10, and corresponds to $\sim 10\%$ of the pp interaction energy at $\sqrt{s} = 40$ TeV, which in turn is 4×10^9 TeV/s. Similarly, for the beam-gas interactions, assuming a residual pressure of 10^{-8} torr nitrogen equivalent in the "warm region" of the evacuated beam pipe and $\sim 4 \times 10^8$ N_2 molecules per cc in the "cold region," the loss rate is $\sim 2 \times 10^4$ p/m/s, which is small compared to the pp interaction rate.

In terms of systematic uncertainties concerning the results of the two previous subsections, it is noteworthy that the inclusion of the magnetic fields in the simulations, in particular for the LBQs, is rather important.

Finally, we note that the relevance of such calculations to the detectors proposed for the study of B-physics (e.g., the FAD apparatus[19]), for various collider luminosities is presented in the section dealing with machine-detector interface issues of these proceedings.[20]

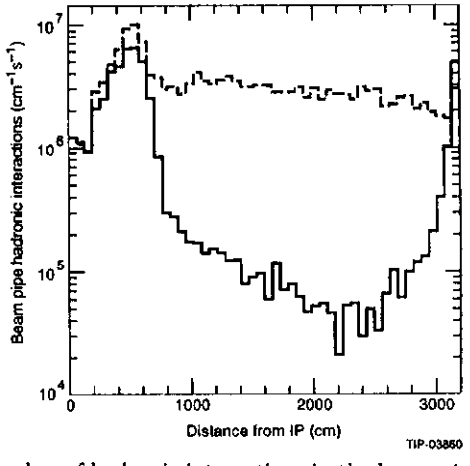

Figure 9. Average number of hadronic interactions in the beam pipe as a function of the longitudinal dimension from the IP, for the GEM apparatus. The dashed line represents a pipe with a constant diameter, and the solid line a pipe with a variable diameter (Reference 2).

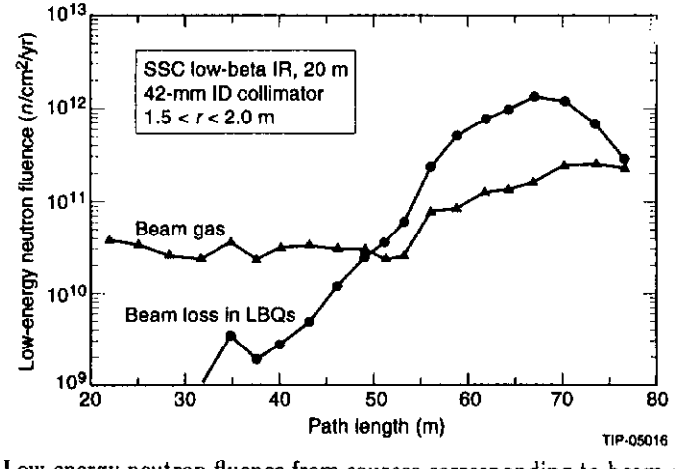

Figure 10. Low-energy neutron fluence from sources corresponding to beam-gas interactions in the beam pipe and beam losses in the collider lattice, in the vicinity of the LBQs. The abscissa refers to the distance from the IP (Reference 18).

3.5 *Parametrization of the Spectrum*

For the purpose of calculating the response of a detector to the background flux of neutrons and photons, it is important to be able to parametrize the energy distribution of these backgrounds obtained from the Monte Carlo simulations. D. Groom[21] has studied this in the context of the background particles' energy distributions that are calculated in the context of the SDC apparatus.[22] As a specific example, Figure 11 (upper figure) shows the spectrum of the neutron flux for the air over the detector itself; the lower figure shows the contributions to the theoretical model used to parametrize the spectrum.

The following essential features of the spectrum have been identified by D. Groom:

- Evaporation peak: this is centered near 0.5 MeV, and is due to the evaporation process of neutrons after the collisions.
- Hole peak: this occurs at approximately 460 keV, and corresponds to an increase in the n-Fe cross section.
- Notch: this is characterized by a sharp peak at 26 keV, and corresponds to a dip in the n-Fe cross section.
- Skirt: this is analogous to a smooth "background" under the spectrum going almost linearly "downhill" from the 500-keV peak to thermal energy values. This is most likely the result of repeated neutron scatterings (downscattering) with some energy loss.
- Thermal peak: this thermal neutron peak is well described by a Maxwellian distribution.

Additional details pertinent to the interpretation of the spectrum can be found in the original document.[21]

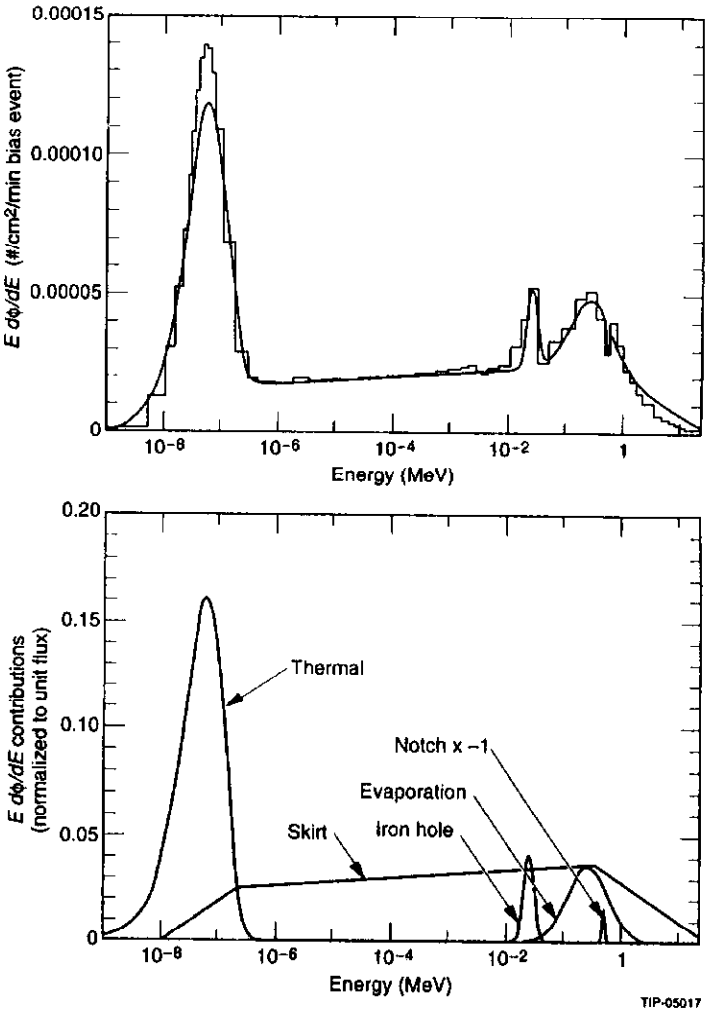

Figure 11. Differential neutron flux spectra corresponding to the "air over the detector" for the SDC apparatus, upper figure (Reference 22). The lower figure indicates the contributions to the theoretical model used to describe the spectra (Reference 21).

3.6 *Charged Particle Fluence and Dose*

In the preceding sections, emphasis has been put on understanding the neutron and photon fluence. In order to be complete, one should also discuss the charged-particle backgrounds as well as the overall issue of dose and activation. For the latter, since the values for the doses and activation levels are specific to the individual detectors, the appropriate details may be found in References 2 and 3 and in References 4 and 5 for the SSC and LHC detectors, respectively.

However, the charged-particle fluence is indeed an important consideration for the silicon detectors proposed for particle tracking and event as well as secondary vertex reconstruction, in particular for the proposed B-physics experiments. In order to obtain a quantitative comparison, Table 3 lists the charged-particle fluences (and corresponding doses) calculated for various luminosities (corresponding to existing and proposed future collider facilities), as a function of the radial distance where it is proposed to implement the silicon devices.

Table 3. List of charged particle fluence (for 10^7 s) from the primary interactions as a function of the perpendicular distance ($r_\perp$) from the IP, for various colliders. The σ's represent the inelastic cross sections.

$r_\perp \rightarrow$	2.5 cm	5.0 cm	10.0 cm	20.0 cm
SSC	19×10^{13}	4.8×10^{13}	1.2×10^{13}	0.3×10^{13}
H: 7.5	part/cm^2	part/cm^2	part/cm^2	part/cm^2
$\mathcal{L}$: 10^{33} cm^{-2}s^{-1}				
σ: 100 mb	5 mrad	1.3 mrad	0.3 mrad	0.08 mrad
LHC	225×10^{13}	56×10^{13}	14×10^{13}	3.5×10^{13}
H: 6.2	part/cm^2	part/cm^2	part/cm^2	part/cm^2
$\mathcal{L}$: 1.7×10^{34} cm^{-2}s^{-1}				
σ: 84 mb	60 mrad	15 mrad	3.7 mrad	0.9 mrad
TEV	0.011×10^{13}	0.003×10^{13}	0.0007×10^{13}	0.0002×10^{13}
H: 3.9	part/cm^2	part/cm^2	part/cm^2	part/cm^2
$\mathcal{L}$: 2×10^{30} cm^{-2}s^{-1}				
σ: 56 mb	2.9×10^{-3} mrad	0.74×10^{-3} mrad	0.18×10^{-3} mrad	0.05×10^{-3} mrad
TEV	0.55×10^{13}	0.14×10^{13}	0.035×10^{13}	0.009×10^{13}
H: 3.9	part/cm^2	part/cm^2	part/cm^2	part/cm^2
$\mathcal{L}$: 10^{32} cm^{-2}s^{-1}				
σ: 56 mb	0.15 mrad	0.04 mrad	0.009 mrad	0.002 mrad

4. EFFECTS ON DETECTORS

The purpose of this section is to present a brief overview concerning the consequences of radiation damage to the operation of silicon detector devices. As indicated in the previous section, these silicon detectors will be placed around the beam pipe, at small radii with respect to the interaction point for purposes of particle track reconstruction and vertex reconstruction. It is beyond the scope of this paper to attempt to summarize the consequences of radiation damage to other detector devices and electronics. Details may be found in recent workshop proceedings.[23]

4.1 *Damage Mechanisms*

The damage mechanisms in silicon devices can essentially be separated into bulk effects and surface effects. The typical energy of the neutrons in the tracking cavity of the apparatus is $\sim$ 1 MeV, characteristic of the nuclear evaporation process. Neutrons in this energy range are effective in creating displacement damage. Figure 12 shows the relative damage of neutrons as a function of the incident n energy, calculated from a knowledge of the n-Si cross sections.[24] Recently, there has been evidence from investigation of electronic devices that the displacement damage is proportional to non-ionizing energy loss (NIEL). This has been calculated by Van Ginneken,[25] and is shown in Figure 13 for different particle species as a function of their incident energy. From this figure it can be ascertained that for a particular value of the incident energy (1–2 MeV), the ratio of the damage coefficient of electrons to neutrons is $\sim 10^{-2}$. Some of the consequences of the bulk damage are:

- an increase in the leakage current of the reverse-biased p-n junction;
- trapping of the mobile charge carriers, leading to incomplete charge collection;
- effective compensation of the material, thus modifying the electrical field characteristics in the device.

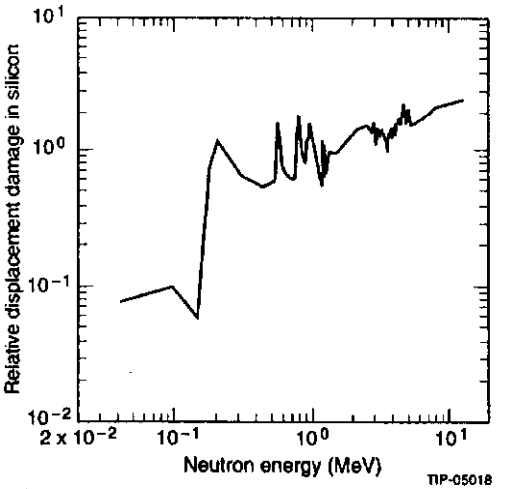

Figure 12. Relative displacement damage by neutrons in silicon, as a function of the neutron energy (Reference 24).

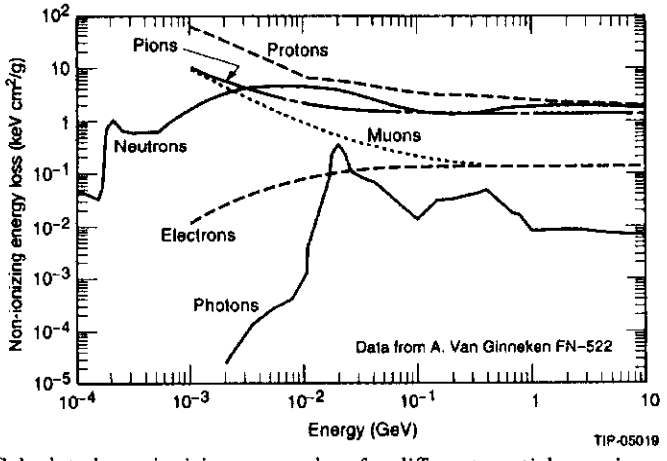

Figure 13. Calculated non-ionizing energy loss for different particle species, as a function of the incident particle energy (Reference 25).

Surface damage affects the passivation layer (SiO_2) and the SiO_2-Si interface region in the p-n junction diode.[23] Also, there could be the creation of "mid-gap" interface states, which are mobile. Likewise, there may be charge trapping due to oxide defects. A partial list of some of the important consequences includes:

- an increase in the surface leakage current;
- a decrease in the charge carrier mobility;
- a decrease in the "interstrip" resistivity of the device;
- the formation of charge "inversion" layers.

These phenomena lead to a degraded performance of the devices. In the following, a brief sample of some of these phenomena is listed.

- Leakage current: an increase in the leakage current of the device will, in turn, lead to an increase in the electronic noise as well as increased power consumption. It is rather well established that the increase in the current density (ΔI) is related to the particle fluence (Φ), as in the expression $\Delta I = \alpha \times \Phi$, where α is referred to as the damage constant. Numerous experiments have measured this constant[23] with different incident particles. Typical values are: $\alpha \simeq 2 \times 10^{-17}$ A/cm for incident neutrons with energy ~ 1 MeV; and $\alpha \simeq 3 \times 10^{-17}$ A/cm for incident protons of energy ~ 800 MeV.
- Effective doping concentration: this is a phenomenon where the initial, n-type (bulk) material gradually becomes intrinsic and then inverts to p-type material with increased particle fluence. The effective donor concentration (N_D) decreases during irradiation as a consequence of the creation of charged damage sites in the bulk. The electric field characteristics, and thus the depletion voltage (V_{dep}), will be affected. The depletion voltage is related to the donor concentration by the equation: $V_{dep} = (e \times N_D \times d^2)/(2 \times \epsilon)$, where e is the electric charge, d is the detector thickness (usually 300 μ), and ϵ is the permittivity of silicon. Figure 14 shows the variation of the depletion voltage as a function of the fluence for 800-MeV incident protons.[26] The phenomenon of "type inversion" occurs at a fluence between 1 and 2×10^{13} p/cm^2. The curves are a fit to the data, using a model in which $N_D = N_o e^{-c\Phi} + \beta\phi$, where N_o is the initial doping concentration, and c and β are coefficients to be determined from the fit to the data points. The model is consistent with a two-component process, which incorporates donor removal and acceptor creation in the silicon bulk. Additional details may be found in Reference 26.

It should be noted that similar conclusions are obtained with incident neutrons, where type inversion is also observed at a fluence of $\sim 2 \times 10^{13}$ n/cm^2.[26] We note, however, that recent results from the RD-2 collaboration[27] at CERN indicate that type inversion is observed at a fluence of $\sim 3 \times 10^{12}$ n/cm^2, which is approximately an order of magnitude lower. It is clear that the systematics concerning the actual neutron fluence have to be quantified. These could be quite large.

The effect of the change in the depletion voltage of the p-n junction device in terms of the charge collection (i.e., peak position) is illustrated in Figure 15. The typical values for the depletion voltage prior to irradiation were in the range $30 < V_{dep} < 65$ V. After irradiation, a bias voltage of 100 V is required to attain the same charge collection.

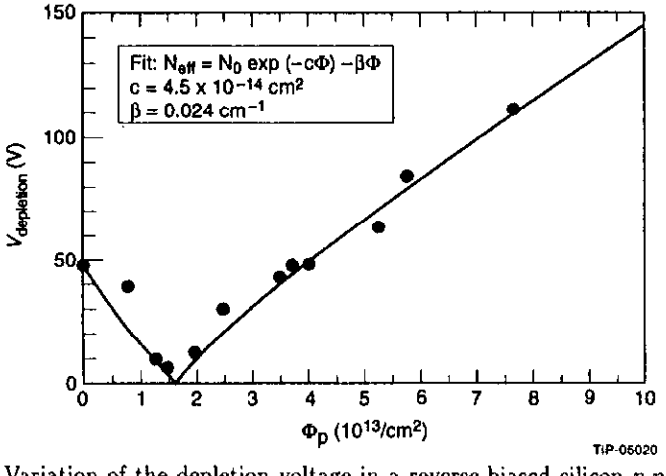

Figure 14. Variation of the depletion voltage in a reverse-biased silicon p-n junction diode as a function of the particle fluence. The solid lines represent a fit to the data in the context of the model described in the text.

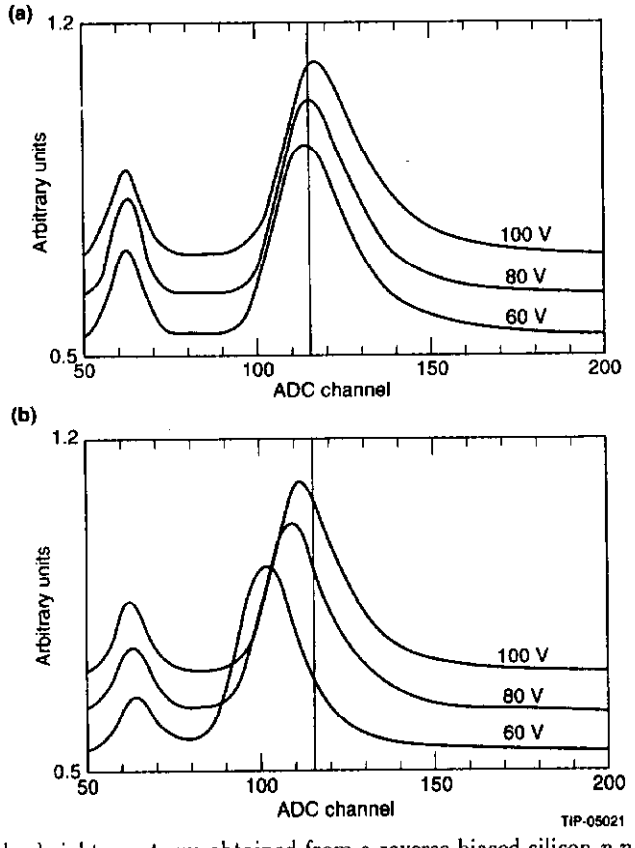

Figure 15. Pulse height spectrum obtained from a reverse-biased silicon p-n junction diode, using a β-source. The upper figure shows the variation in the peak position of the pulse height spectrum for the different applied bias voltages, after the detector has received a fluence of 1.7×10^{12} n/cm^2. In analogy, the lower figure shows the same, but for a larger fluence corresponding to 6×10^{12} n/cm^2. The detectors are required to be significantly overdepleted after irradiation with respect to the original values in order to ensure complete charge collection.

4.2 Consequences for Operation

The silicon devices operating at the SSC, with the nominal luminosity of 10^{33} cm^{-2}s^{-1}, will be exposed to a fluence of $\sim 10^{14}$ particles/cm^2 over approximately a decade of operation, at a typical radius of 10 cm from the interaction point. The consequences of radiation damage suggest that it would be desirable to operate the devices at relatively low temperatures (0°C) as compared to ambient temperature. The reason is essentially that the leakage current is lowered by a factor two for every 7°C reduction in the temperature. Thus, experimental results[28] suggest that, for example, operating the devices at 0°C as opposed to 24°C would lead to approximately a factor 10 reduction in the leakage current. Even if one takes into account the lack of annealing at 0°C, the overall reduction in the leakage current would be a factor ~ 5, with respect to the higher temperature. Likewise, from the point of view of the operating voltage, the experimental observations favor the lower temperature. It is important to stress that the study of the annealing phenomenon and its temperature dependence is the subject of extensive investigation at present. The annealing phenomenon is rather complicated, and the characteristic time constants involved can be long (of the order of hundreds of days), requiring large time periods of monitoring and analysis. Further details and an update on recent experimental results can be found in Reference 28.

5. ACKNOWLEDGEMENTS

It is a pleasure to acknowledge my colleagues from the GEM experiment neutron task force and the SDC experiment neutron task force. In particular, I am most grateful to T. Gabriel, D. Groom, V. Kubarovsky, N. Mokhov, and L. Waters for their valuable guidance.

6. REFERENCES

1. D. E. Groom, *Nucl. Instr. and Meth.* **A279** (1989) 1.
2. Technical Design Report, GEM Experiment, SSCL-SR-1219 (1993).
3. Technical Design Report, SDC Experiment, SSCL-SR-1215 (1992).
4. Letter of Intent, ATLAS Experiment, CERN/LHCC/92-4 (1992).
5. Letter of Intent, CMS Experiment, CERN/LHCC/92-3 (1992).
6. Y. M. Nosochkov, these Proceedings.
7. D. E. Groom, ed., SSC Report SSC-SR-1033 (1988).
8. J. Ranft et al., UL-92-7 and UL-HEP-93-01, Leipzig, Germany.
9. D. E. Groom, SDC Report SDC-93-448 (1993); and references contained therein.
10. M. Barbier, *Induced Radioactivity*, North-Holland Publishing Company (1969).
11. Radiation calculations using LAHET/MCNP/CINDER 90, LANL Report LA-UR-89-3014 (1992); and references contained therein.
12. T. A. Gabriel et al., ORNL Report ORNL/TM-5619 (1977); and references contained therein.
13. A. Ferrari et al., in *Proceedings of the Second International Conference on Calorimetry in High Energy Physics*, p. 101 (1991); and references contained therein.
14. C. Zeitnitz and T. A. Gabriel, private communication. R. Brun et al., CERN-DD/78/2 (1978); and references contained therein.
15. N. Mokhov, Fermilab report FNAL-FN-509 (1989); and references contained therein.
16. V. Kubarovsky, private communication.
17. G. R. Stevenson, *Nucl. Instr. and Meth.* (Proc. Suppl.) **32** (1993) 37.
18. N. Mokhov, private communication; and N. Mokhov in the collected minutes of the SSCL Collider-Detector interface meetings (1993).
19. J. D. Bjorken, *Inter. Jour. of Mod. Phys.*, **A7**, N18 (1992) 4189.

20. V. Bharadwaj (ed.), these proceedings.

21. D. E. Groom, SDC Report SDC-93-492 (1993).

22. A. Palounek et al., SDC Report SDC-93-467 (1993).

23. G. Hall, CERN-LHC Report CERN 90-10 (1990); and T. Dombeck et al., (eds.), in *Proceedings of the Symposium on Detector Research and Development for the Superconducting Super Collider*, Fort Worth, Texas (1990); and references contained therein.

24. J. E. Gover and J. R. Srour, Sandia Lab. Report SAND85-0776 (1985).

25. A. Van Ginneken, Fermilab Note FN-522 (1989).

26. A. Weinstein et al., SDC Report SDC-91-133 (1991); and references contained therein.

27. The RD-2 Collaboration Status Report: CERN/DRDC/93-18, March 1993.

28. H. Ziock et al., "Temperature dependence of the radiation induced change of depletion voltage in silicon PIN detectors." In preparation.